Comparison of XFEM and Voxelbased FEM for the Approximation of Discontinuous Stress and Strain at Material Interfaces

T. Zangmeister, H. Andrä, R. Müller

When analyzing bimaterial problems, often stress concentrations appear close to material interfaces and cause nonlinear effects like damage or plastic yielding. Therefore, a precise approximation of stresses at interfaces is desirable. However, jumps in material parameters lead to non-smooth solutions (i.e. kinks in the displacements and jumps in the stresses and strains), which reduce the accuracy of standard discretization methods including the finite element method (FEM). The popular extended finite element method (XFEM) belongs to the class of methods, where additional unknowns are introduced to approximate jumps of the unknowns on meshes which are not aligned to the interface or boundaries. The field of application is the stress analysis of microstructures of two-phase materials with high contrast between the phases including nonlinear effects. The focus of this paper is to considers the XFEM approximation quality of strains and displacements at material interfaces. XFEM and standard FEM solutions are compared for varying mesh sizes. Therefore an analytical solution for a spherical inclusion in a finite domain under specific loading conditions is considered. This analytical solution is then compared in detail to different finite element discretizations with standard FEM and XFEM.

1 Introduction

The discretization error of the FEM depends, roughly speaking, on both the approximation error of the finite element shape functions and the numerical quadrature error. The latter quadrature error itself depends usually mainly on deviations of the finite element boundaries from exact domain boundaries or from material interfaces because the domain of integration is only approximately captured. The isogeometric FEM is one approach to reduce this part of the discretization error. Nevertheless, in many applications with non-smooth boundaries and material interfaces isogeometric finite elements or at least piecewise linear approximations of all boundaries and interfaces lead to an undesired effort for the mesh generation. For these cases Belytschko and Black (1999) and Moës et al. (1999) introduced the extended finite element method (XFEM) which is able to include discontinuities into the finite element shape functions with the help of additional degrees of freedom. Therefore, XFEM allows to capture kinks in the unknown displacements and jumps in the derivatives of the unknowns within the interior of finite elements. There is no need of interface aligned meshes anymore, and advantages of regular meshes can be exploited. Immersed interface and immersed boundary methods belong to the same class of methods, see Rutka et al. (2006), but will not be discussed in this paper.

2 Mathematical Model

2.1 Dirichlet Boundary Value Problem in Linear Elasticity

A bounded Lipschitz domain $\Omega \subset \mathbb{R}^3$ with kinematic boundary conditions on the boundary $\partial\Omega$ is given. The Dirichlet boundary value problem for the unknown displacements $\boldsymbol{u}$ is defined by

$$\nabla \cdot \boldsymbol{\sigma}(\boldsymbol{u}) = \boldsymbol{0} \ \text{in } \Omega, \tag{1}$$

$$\boldsymbol{\sigma}(\boldsymbol{u}) = \mathbb{C} : \boldsymbol{\varepsilon}(\boldsymbol{u}) \ \text{in } \Omega, \tag{2}$$

$$\boldsymbol{\varepsilon}(\boldsymbol{u}) = \frac{1}{2}\left[\nabla\boldsymbol{u} + (\nabla\boldsymbol{u})^T\right] \ \text{in } \Omega, \tag{3}$$

$$\boldsymbol{u} = \overline{\boldsymbol{u}} \ \text{on } \partial\Omega, \tag{4}$$

where ∇ represents the nabla operator, '·' denotes the scalar product, $\boldsymbol{\sigma}$ denotes the stress tensor, $\mathbb{C}$ stands for the fourth order elastic stiffness tensor. The stress is computed according to Hooke's law, cf. Eq. (2) with the linearized strain tensor ε. The given Dirichlet data are denoted by $\overline{\boldsymbol{u}}$. Eq. (1) describes the equilibrium condition and Eq. (4) specifies the Dirichlet boundary conditions. Eq. (3) shows the linearized kinematic relation between displacement and strain. Let us now consider the Sobolev space $\mathcal{V} := [H^1(\Omega)]^3$ of vector-valued functions whose components are square-integrable with weak first-order partial derivatives in the Lebesgue space $L_2(\Omega)$. We define the subspace

$$\mathcal{V}_0 := \left\{ \boldsymbol{v} \in [H^1(\Omega)]^3 : \boldsymbol{v} = \boldsymbol{0} \text{ on } \partial\Omega \right\} \subset \mathcal{V} \tag{5}$$

and the manifold

$$\mathcal{V}_* := \left\{ \boldsymbol{v} \in [H^1(\Omega)]^3 : \boldsymbol{v} = \overline{\boldsymbol{u}} \text{ on } \partial\Omega \right\}, \tag{6}$$

with $\overline{\boldsymbol{u}}$ from Eq. (4).

The weak form of Eq. (1) is given by: Find $\boldsymbol{u} \in \mathcal{V}_*$ such that

$$\int_\Omega (\mathbb{C} : \boldsymbol{\varepsilon}(\boldsymbol{u})) : \boldsymbol{\varepsilon}(\delta\boldsymbol{u}) \, d\boldsymbol{x} = 0, \tag{7}$$

holds for all $\delta\boldsymbol{u} \in \mathcal{V}_0$. The Dirichlet problem (7) has a unique solution.

2.2 Discretization

The finite element discretization of (7) is sketched shortly by using the usual matrix notation, see e.g. Gross et al. (1990) and Zienkiewicz and Taylor (2000). The standard Voigt notation is used for rewriting 2nd order tensors as vectors and 4th order tensors as matrices. We introduce a quasi-uniform tetrahedral finite element mesh with the mesh size h, i.e. h is the diameter of the circumsphere of the tetrahedron. The corresponding approximate solution for the displacement, strain and stress is denoted by $\boldsymbol{u}_h, \boldsymbol{\varepsilon}_h$ and $\boldsymbol{\sigma}_h$, respectively. Next the matrix $\boldsymbol{N}$ of linear (or quadratic) shape functions for the displacements and the nodal displacement vector $\boldsymbol{d}$ is introduced, so that

$$\boldsymbol{u}_h(\boldsymbol{x}) = \boldsymbol{N}(\boldsymbol{x})\boldsymbol{d} \in \mathcal{V}_*. \tag{8}$$

The corresponding strain field is defined by

$$\boldsymbol{\varepsilon}(\boldsymbol{u}_h) = \frac{1}{2} \left[\nabla\boldsymbol{u}_h + (\nabla\boldsymbol{u}_h)^T \right] = \boldsymbol{S}\boldsymbol{N}(\boldsymbol{x})\boldsymbol{d} =: \boldsymbol{B}(\boldsymbol{x})\boldsymbol{d} \tag{9}$$

with the symmetric gradient operator

$$\boldsymbol{S} = \begin{pmatrix} \frac{\partial}{\partial x} & 0 & 0 \\ 0 & \frac{\partial}{\partial y} & 0 \\ 0 & 0 & \frac{\partial}{\partial z} \\ \frac{\partial}{\partial y} & \frac{\partial}{\partial x} & 0 \\ 0 & \frac{\partial}{\partial z} & \frac{\partial}{\partial y} \\ \frac{\partial}{\partial z} & 0 & \frac{\partial}{\partial x} \end{pmatrix}. \tag{10}$$

The virtual displacements $\delta\boldsymbol{u}_h$ can be written as

$$\delta\boldsymbol{u}_h(\boldsymbol{x}) = \boldsymbol{N}(\boldsymbol{x})\delta\boldsymbol{d} \in \mathcal{V}_0. \tag{11}$$

and hence

$$\boldsymbol{\varepsilon}(\delta\boldsymbol{u}_h) = \boldsymbol{B}(\boldsymbol{x})\delta\boldsymbol{d}. \tag{12}$$

The stiffness or elasticity tensor $\mathbb{C}$ is hereinafter referred to as $\boldsymbol{D}$ in Voigt notation. Next we plug in $\boldsymbol{u}_h$ in the left-hand side (7) to obtain

$$\int_\Omega (\mathbb{C} : \boldsymbol{\varepsilon}(\boldsymbol{u}_h)) : \boldsymbol{\varepsilon}(\delta\boldsymbol{u}_h) \, dx = \int_\Omega (\boldsymbol{B}(\boldsymbol{x})\delta\boldsymbol{d})^T \boldsymbol{D}(\boldsymbol{B}\boldsymbol{d}(\boldsymbol{x})) \, dx =: \delta\boldsymbol{d}^T \boldsymbol{K} \, \boldsymbol{d}, \tag{13}$$

where the stiffness matrix $\boldsymbol{K}$ is defined by

$$\boldsymbol{K} = \int_\Omega \boldsymbol{B}^T(\boldsymbol{x})\boldsymbol{D}\boldsymbol{B}(\boldsymbol{x}) \, d\boldsymbol{x}. \tag{14}$$

Eq. (7) leads to the discretized equilibrium condition

$$(\delta\boldsymbol{d}^T)(\boldsymbol{K}\boldsymbol{d}) = 0. \tag{15}$$

As Eq. (15) must hold for all virtual displacements $\delta\boldsymbol{d} \in \mathcal{V}_0$, we obtain an homogeneous linear system of equations

$$\boldsymbol{K}\boldsymbol{d} = \boldsymbol{0} \tag{16}$$

with positive definite symmetric matrix $\boldsymbol{K}$ and unknown nodal displacement vector $\boldsymbol{d}$. The resulting linear system has a unique solution in $\mathcal{V}_*$. For numerical procedures for solving FEM type equation systems we refer to Axelsson and Barker (1984).

2.3 Mesh Discretization Techniques

In FEM, a finite element mesh has to be generated first. In this investigation two different discretization strategies are compared with each other. The first is referred to as FEM with a voxel-based mesh and the second as XFEM combined with the level set method. For both approaches we assume that there exists an analytical description of the bimaterial volume. If this is not the case we refer to Lian et al. (2012), where a novel approach for a level set creating segmentation process is introduced.

For the first approach an initial voxel-based mesh is generated. The material number of a given element is then selected according to the material phase found at the centroid of this particular element. As previously stated the FEM gives best results when the underlying mesh conforms to the geometry with smooth representations of physical surfaces within the discretized volume (cf. for example Lian et al. (2012)). As we use a voxel based approach to represent surfaces that are not aligned according to the underlying voxel mesh we expect intrinsic jagged surfaces. This results in high local stress oscillations (cf. Guldberg et al. (1998)). For many applications (e.g. modeling of plastic yielding or damage) it is crucial to reduce errors in the stress field close to the interfaces and to accurately model the stress jump across the material interface.

A standard way of doing so, is to adapt the mesh in such a way that it conforms to the underlying geometry. Another possible way of taking the geometry into account is the use of the eXtended Finite Elements Method (XFEM) (introduced by Belytschko and Black (1999) and Moës et al. (1999), cf. Fries and Belytschko (2010)) combined with the level set method (cf. Osher and Sethian (1988) and Sethian (1999)). The XFEM was first combined with the level set method by Belytschko et al. (2001) and Stolarska et al. (2001). There exists a variety of different level set functions. Here we will use the signed distance function. Assume the surface Γ divides the volume Ω into two different parts which we will refer to as an inclusion Ω_I and a matrix Ω_M. The following scalar function then is called signed distance function

$$\Phi_I : \Omega \subset \mathbb{R}^3 \to \mathbb{R} : \Phi(\boldsymbol{x}) = \begin{cases} \min\limits_{\boldsymbol{y}\in\Gamma} \|\boldsymbol{x}-\boldsymbol{y}\|, & \boldsymbol{x} \in \Omega_M \\ 0, & \boldsymbol{x} \in \Gamma \\ -\min\limits_{\boldsymbol{y}\in\Gamma} \|\boldsymbol{x}-\boldsymbol{y}\|, & \boldsymbol{x} \in \Omega_I \end{cases} . \tag{17}$$

Common to all level set functions is that its zero isosurface describes a surface in 3D that is of special interest. The set of all points on the material interface then is equal to $\Gamma = \{\boldsymbol{x} \in \Omega \mid \Phi(\boldsymbol{x}) = 0\}$. When handling more than a single inclusion Ω_I, a global level set function may be defined as $\Phi = \min\limits_I \Phi_I$. The XFEM now makes use of the a priori knowledge that at the material interface there are kinks in the displacement field and jumps in the strain field without the need of adopting the mesh to the geometrical information of the interface. This is done by adding an enrichment term to the standard FEM discretization of the solution function, see Eq. (8). The displacement field is now approximated by

$$\boldsymbol{u}_h^{\text{xfem}}(\boldsymbol{x}) = \underbrace{\sum_{i\in J} N_i(\boldsymbol{x})\boldsymbol{d}_i}_{\text{classical FEM ansatz}} + \underbrace{\sum_{i\in J^*} N_i(\boldsymbol{x})\boldsymbol{a}_i F(\boldsymbol{x})}_{\text{enrichment term}} \in \mathcal{V}_*. \tag{18}$$

In Eq. (18), J reqresents the index set of nodes of the finite element mesh, J^* denotes the index set of all nodes attached to at least one element which is intersected by the material interface, $\boldsymbol{d}_i$ describes the unknown displacement of node i. The function $F(\boldsymbol{x})$ characterizes the enrichment function which specifies the type and position of the discontinuity within the element of interest. In the case considered here, a kink in the displacement field at the material interface. The variable $\boldsymbol{a}_i$ represents additional enrichment unknowns which describe the exact

value, slope etc of the discontinuity within the element of interest. Depending on the choice of $F(\boldsymbol{x})$ different scenarios can be modeled, but as we focus attention to the bimaterial problem a good choice for $F(\boldsymbol{x})$ is the so called "modified abs enrichment" introduced in Moës et al. (2003)

$$F(\boldsymbol{x}) = \sum_{i \in K(\boldsymbol{x})} N_i(\boldsymbol{x}) |\Phi(\boldsymbol{x}_i)| - \left| \sum_{i \in K(\boldsymbol{x})} N_i(\boldsymbol{x}) \Phi(\boldsymbol{x}_i) \right| \tag{19}$$

as it circumvents problems with blending elements which shall not be discussed at this point (the interested reader is referred to Fries and Belytschko (2010)). The index set $K(\boldsymbol{x})$ represents the set of all nodes of the element that contains point $\boldsymbol{x}$. Combining equations (18) and (19) yields

$$\boldsymbol{u}_h^{\text{xfem}}(\boldsymbol{x}) = \sum_{i \in J} N_i(\boldsymbol{x}) \boldsymbol{d}_i + \sum_{i \in J^*} N_i(\boldsymbol{x}) \boldsymbol{a}_i \left(\sum_{j \in K(\boldsymbol{x})} N_j(\boldsymbol{x}) |\Phi(\boldsymbol{x}_j)| - \left| \sum_{j \in K(\boldsymbol{x})} N_j(\boldsymbol{x}) \Phi(\boldsymbol{x}_j) \right| \right). \tag{20}$$

It shall be emphasized that the previously introduced discretization scheme remains the same in principal. Only the number of unknowns has changed and the shape function matrix $\boldsymbol{N}$ for enriched nodes is more complicated as well as the symmetric gradient matrix $\boldsymbol{B}$. In the following we will compare the two approaches.

3 Comparison of FEM and XFEM close to Material Interface

3.1 Analytical Reference Example

For a detailed comparison between standard FEM and XFEM we chose a classical Eshelby problem (cf. Eshelby (1957)) as this will serve us as an analytical reference solution for a specific bimaterial problem. Consider an infinitely extended material Ω that has a single spherical inclusion Ω_I. Let both materials have the same Poisson's ratio $\nu := \nu_{\text{M}} = \nu_{\text{I}}$. The bulk modulus of the inclusion shall be denoted with K_{I} and the bulk modulus of the surrounding matrix with K_{M}. Let us denote an applied strain at infinity by $\varepsilon^0 = \epsilon \, \mathbf{1}$ as a strain field without a deviatoric part, with the identity tensor $\mathbf{1}$. From Mura (1987) it is known that the corresponding equivalent eigenstrain ε^* in the spherical inclusion then is computed via

$$\varepsilon^* = \frac{(K_{\text{I}} - K_{\text{M}}) \, \text{tr} \, (\varepsilon^0)(1 - \nu)}{(4\nu - 2)K_{\text{M}} - (1 + \nu)K_{\text{I}}} \mathbf{1}, \tag{21}$$

with the trace operator tr. Let us consider the following material parameters

$$E_{\text{M}} = 1 \text{ MPa}, \ E_{\text{I}} = 10 \text{ MPa and } \nu_{\text{M}} = \nu_{\text{I}} = 0.3. \tag{22}$$

which results in

$$K_{\text{M}} = 5/6 \text{ MPa and } K_{\text{I}} = 25/3 \text{ MPa}. \tag{23}$$

Additionally let $\epsilon = 0.01$. Inserting these parameters into Eq. (21) yields

$$\varepsilon^* = \frac{3(K_{\text{I}} - K_{\text{M}})\epsilon(1 - \nu)}{(4\nu - 2)K_{\text{M}} - (1 + \nu)K_{\text{I}}} \mathbf{1} = -\frac{63}{4600} \mathbf{1} \tag{24}$$

as the equivalent eigenstrain in Ω_I for an equivalent homogenous material. As this strain ε^* is purely volumetric another result from Eshelby (cf. Eshelby (1957) or Mura (1987)) can be used. The radial displacement in this equivalent inclusion problem is known to be equal to

$$u_r = \frac{1 + \nu}{1 - \nu} \frac{1}{r^2} \int_0^r \epsilon^* \xi^2 \, d\xi \tag{25}$$

where r is the distance from the center of the sphere and ϵ^* denotes the radial component of the volumetric strain ε^*. When denoting the radius of the sphere with a, Eq. (25) becomes for $r > a$

$$u_r = \frac{1 + \nu}{1 - \nu} \frac{1}{r^2} \left(\int_0^a \epsilon^* \xi^2 \, d\xi + \int_a^r 0 \, d\xi \right) = -\frac{39a^3}{4600r^2}, \tag{26}$$

as the equivalent eigenstrain vanishes outside of the sphere.

Now consider a spherical inclusion in a finite volume, in this case a cube with a sphere in its center with the diameter of the sphere being $l := 2a$, which is half of the length of the cube. When superimposing this equivalent eigenstrain with the applied strain at infinity ε^0, Eq. (26) provides us the possibility to specify displacement boundary conditions on the geometry such that the strain field will be equal to the strain field in the vicinity of the sphere in an infinitely extended material described earlier. Thus for any $\boldsymbol{x} \in \Omega$ with a distance r from the center of the sphere, the radial displacement equals

$$u_r(\boldsymbol{x}) = \left\{ \begin{array}{ll} r\epsilon - \frac{39r}{4600}, & \boldsymbol{x} \in \Omega_I \\ r\epsilon - \frac{39l^3}{36800r^2}, & \boldsymbol{x} \in \Omega\backslash\Omega_I. \end{array} \right. \tag{27}$$

When imposing this radial displacement everywhere on the boundary $\partial\Omega$ of the RVE the radial strain in Ω_I is

$$\varepsilon_r = \frac{1+\nu}{3(1-\nu)}\epsilon^* + \epsilon \approx 0.00152174. \tag{28}$$

In $\Omega\backslash\Omega_I$ the radial strain becomes

$$\varepsilon_r = -\frac{2(1+\nu)}{3(1-\nu)}\frac{a^3}{r^3}\epsilon^* + \epsilon \approx 0.0169565\frac{a^3}{r^3} + 0.01. \tag{29}$$

Fig. 1 shows a plot of the analytical solution for the radial strain across the material interface. As already stated, the radial strain within the sphere is constant, at the material interface there is a jump, and in the matrix the radial strain decays proportional to r^{-3}. The diameter of the sphere is chosen to be half of the width of the representative volume element (RVE) and the sphere is positioned in the center of the RVE.
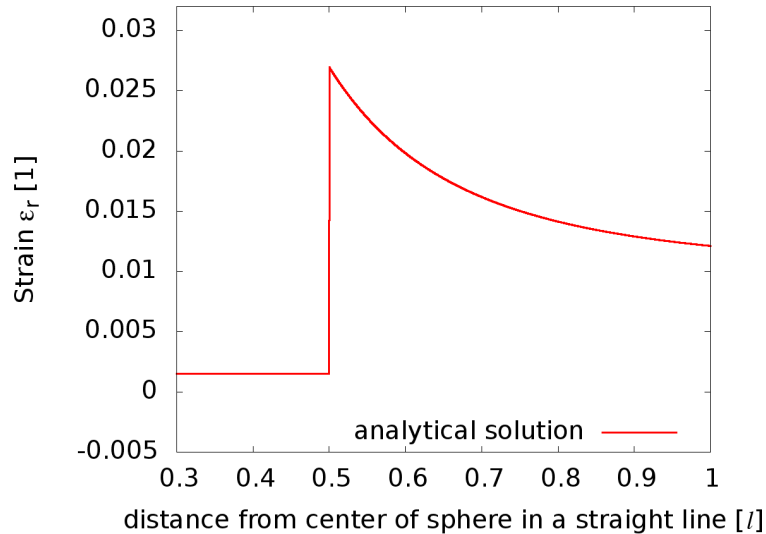

Figure 1: Analytical solution for radial strain

As the underlying mesh we chose a regular tetrahedral mesh created from a voxelized image of the sphere discretized with four different mesh parameters $h_1 = 2^{-3}l$, $h_2 = 2^{-4}l$, $h_3 = 2^{-5}l$ and $h_4 = 2^{-6}l$. The mesh corresponding to h_1 consits of 16^3 voxels, h_2 corresponds to 32^3 voxels, h_3 corresponds to 64^3 voxels and h_4 corresponds to 128^3 voxels. In Fig. 2 cross sections from the meshes with mesh parameter $h_1 = 2^{-3}l$ are shown. Fig. 2 a) displays the mesh used for both standard FEM and XFEM. The material colors are set according to the level set function. It can be easily seen that the material interface does not coincide with element faces. In Fig. 2 b) the elements containing the material interface are colored in dark red. These are the elements with need the extra enrichment for the XFEM and hence defines the set J^* introduced in Eq. 18. J^* is the set of all nodes attached to at least one element which is intersected by the material interface. Obviously when computing the stiffness matrix from Eq. 14, the local elasticity tensor depends on the material. Hence, when integrating Eq. 14 in the elements containing the interface, special emphasis has to be put on the local elasticity tensor. In this work this has been taken care of by splitting up the interface elements into subtetrahedrons for the numerical integration. This

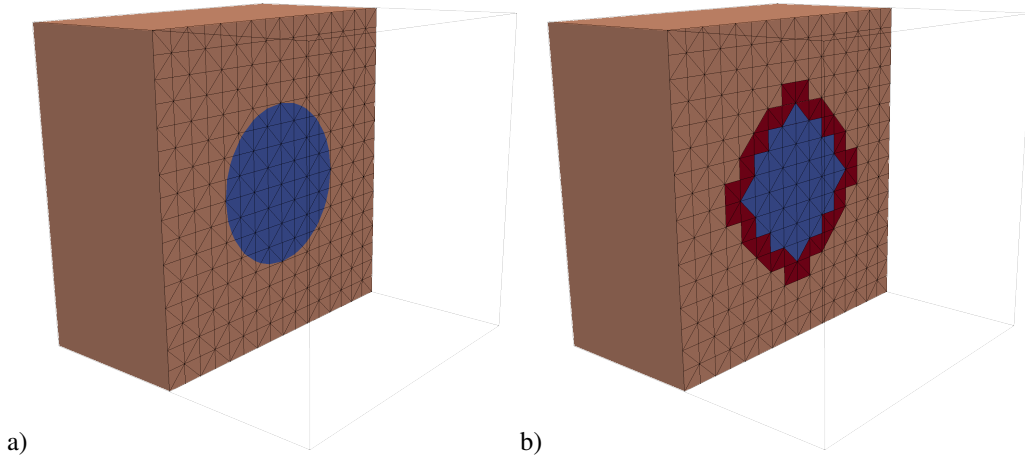a)   b)

Figure 2: Discretization example for XFEM and standard FEM on mesh with $h_1 = 2^{-3}l$

is done according to the underlying level set function with linear ansatz functions. That is, the level set values are evaluated exactly at at each grid point of the underlying mesh and approximated linearly in between. The sphere shown in Fig. 2 is plotted according to these linear approximation of the level set function.

The interface elements are either split into four or six subtetrahedrons, depending on how the four nodes of the element are separated into the two material phases. As we choose in the standard FEM approach linear shape functions for finite element mesh, one Gaussian point per subtetrahedron is required. For the XFEM with linear shape functions the numerical integration has to be performed with a quadratic Gaussian quadrature rule which results in 4 Gaussian points per subtetrahedron. This is due to the quadratic terms in Eq. 20. Fig. 3 shows the same

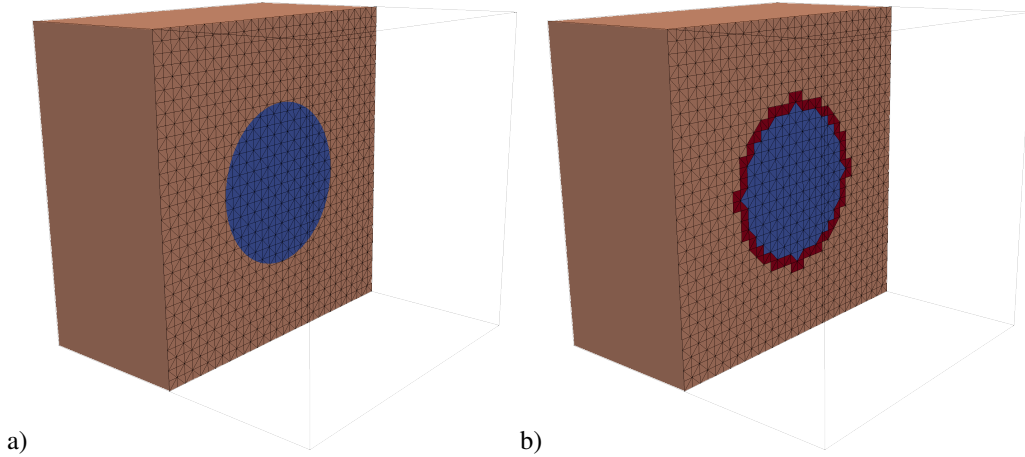a)   b)

Figure 3: Discretization example for XFEM and standard FEM on mesh with $h_2 = 2^{-4}l$

geometry as in Fig. 2, but discretized with a different mesh parameter $h_2 = 2^{-4}l$. It strikes that the number of interface elements increase. It is also obvious that it does not increase as fast as the total number of elements in the mesh does, compared to Fig. 2. The exact figures of the computational effort created by the enriching technique is summarized in Table 1.

mesh parameter h	$2^{-3}l$	$2^{-4}l$	$2^{-5}l$	$2^{-6}l$
number of elements	20,480	163,840	1,310,720	10,485,760
number of enriched elements	1,160	4,472	18,236	73,652
number of nodes	4,913	35,937	274,625	2,146,689
number of enriched nodes	436	1,660	6,744	27,216
number of Gaussian points standard FEM	25,284	182,930	1,388,617	10,800,411
number of Gaussian points XFEM	39,696	240,200	1,622,308	11,744,364

Table 1: Computational effort for different mesh parameters h

3.2 Simulation Results

The simulations described in the following have all been computed with FeelMath (Finite Elements for Elastic MATerials and Homogenization) an inhouse software project at Fraunhofer ITWM.

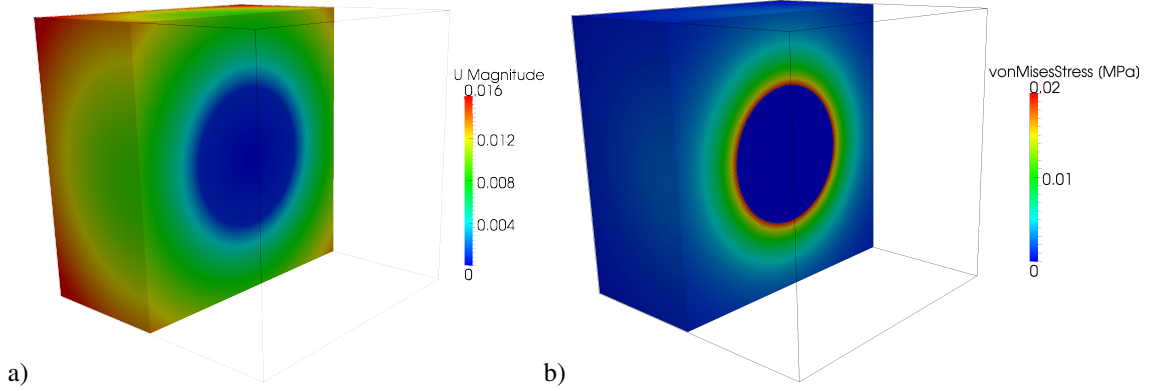

a)   b)

Figure 4: Simulation results for XFEM with mesh parameter $h_4 = 2^{-6}l$: a) displacement field and b) von Mises equivalent stress in MPa

Fig. 4 shows the magnitude of the displacement field and the von Mises equivalent stress σ_v for one of the simulations. The von Mises equivalent stress is defined as $\sigma_v = \sqrt{3J_2}$ with J_2 the second invariant of the stress deviator. As the imposed displacement boundary conditions correspond to a purely radial strain, it is not surprising to find the solution being a radial displacement field. We already stated in the previous section that the strain in the spherical inclusion is constant and its deviatoric part is equal to $\mathbf{0}$. Hence the von Mises stress inside the spherical inclusion must equal zero, which is recovered in the simulation. The jump in the stress field across the material interface is quite pronounced in Fig. 4. Nevertheless the focus of this work is on the correct approximation of the jump in the strain field and the accuracy with regard to the analytical solution. In order to do so, we analyze the strain tensor along different orientations. The origin of all lines is the center of the sphere and they reach out in different angles. Along each line the normal component of the strain is analyzed.
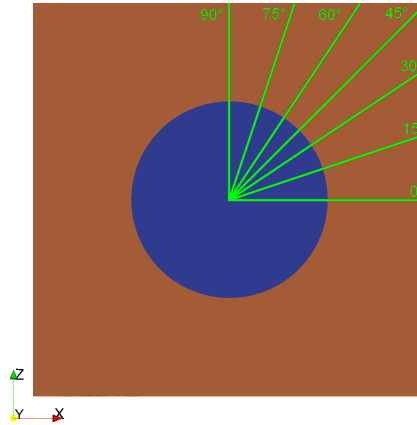

Figure 5: Visualization of different lines in a 2D cross section

Fig. 5 shows some of these lines in a 2D cross section of the 3D volume. Due to symmetry reasons only one eights of the volume is analyzed. The orientation of each line is described by two angles. Analogously to standard spherical coordinates, the first angle describes the angle in the x-y-plane (polar angle), the second angle denotes the angle in the x-y-plane (azimuth angle). For both angles a stepsize of $15°$ has been chosen such that for one eights of the sphere, 43 different lines have been analyzed. These lines can be imagined as rays starting from the center of the sphere that pass through the whole volume. Fig. 6 – Fig. 9 plot the normal component of the strain tensor along such lines over the distance to the center of the sphere. As we chose tetrahedrons with linear shape functions (with and without XFEM enrichements) as the base elements of our finite element mesh, the solution for the strains is constant in each element. In the following plots, XFEM results will always be plotted with 'x' as tickmarks and standard FEM with 'o'. The tickmarks along these lines have been set at each beginning of a new element intersected by the line.

137

As a first example, with x-z-angle=0° and x-y-angle=15° we chose the line that is tilted by 0° away from the x axis in the x-z-plane and 15° in the x-y-plane, respectively.
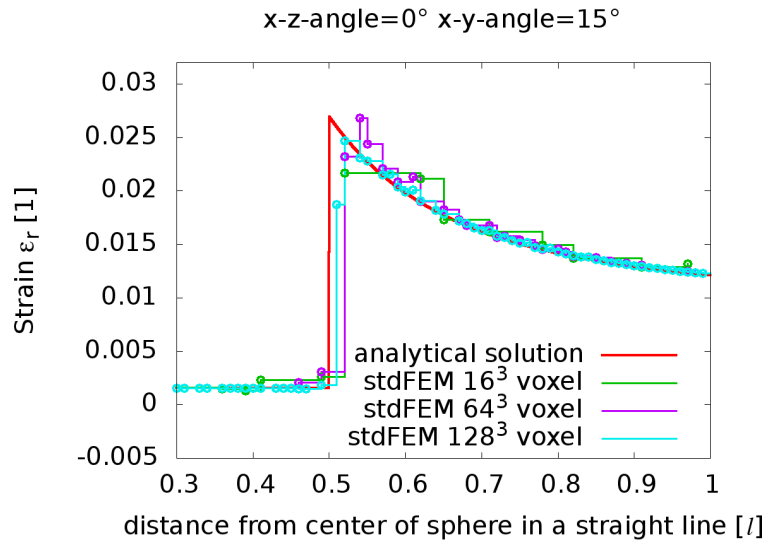

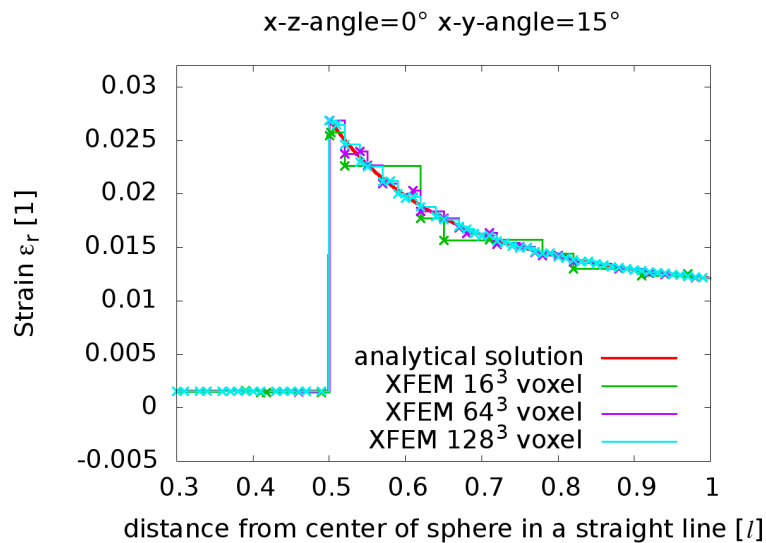Figure 6: Normal strain component along line with x-y-angle=15° and x-z-angle=0° for standard FEM

Figure 7: Normal strain component along line with x-y-angle=15° and x-z-angle=0° for XFEM

In Fig. 6 and Fig. 7 it can be seen, that the analytical solution is approximated well. In both cases (similar to every single other case analyzed in this study) the radial strain within the spherical inclusion is reproduced more or less exactly. The jump at the interface is approximated rather well. Not surprisingly the standard FEM is not reproducing the exact jump but underestimating it. This was the case in the vast majority of the analyzed examples. As in almost every single case in this study, the XFEM reproduces the jump significantly better. Special emphasis shall be put on the XFEM reproducing the analytical solution rather well already with a comparatively coarse grids with a large mesh parameter h. It is also striking that the difference in the result between the two methods vanishes away from the interface. Nevertheless the results of the two methods differ in the vicinity of the material interface. With a decreasing mesh parameter h, the difference between numerical results and analytical solution reduces.

The effect that standard FEM is mostly underestimating the exact jump at the material interface seems to have a simple explanation: the handling of the interface elements with a special integration rule but linear shape functions over the whole element. As these elements have been integrated via subtetrahedrons with piecewise constant

material parameters, the interface elements act similar to a small layer of some interface material with some mean Young's modulus. The exact value of the resulting Young's modulus depends on the volume percentage of the different materials in the interface elements only. Nevertheless when introducing a different integration rule without taking the subtetrahedrons into account lead to similar results, especially the general underestimation of the jump at the interface. Hence, different integration rules will not be discussed further in this work.
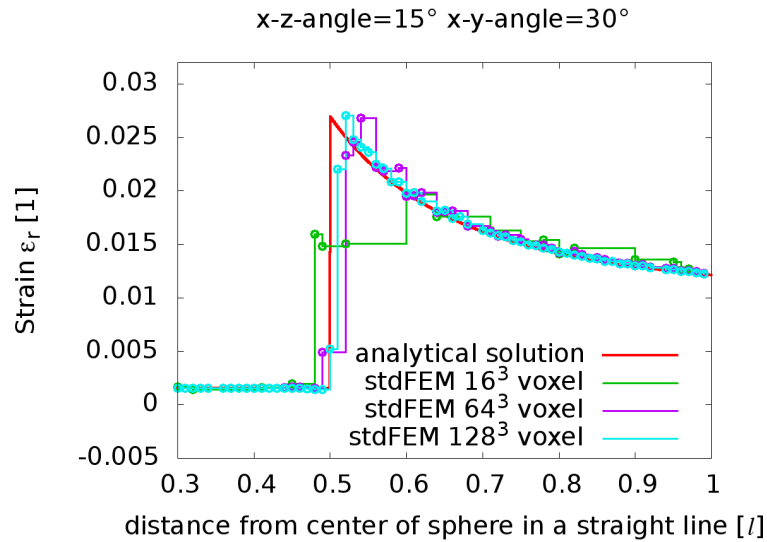

Figure 8: Normal strain component along line with x-y-angle=30° and x-z-angle=15° for standard FEM
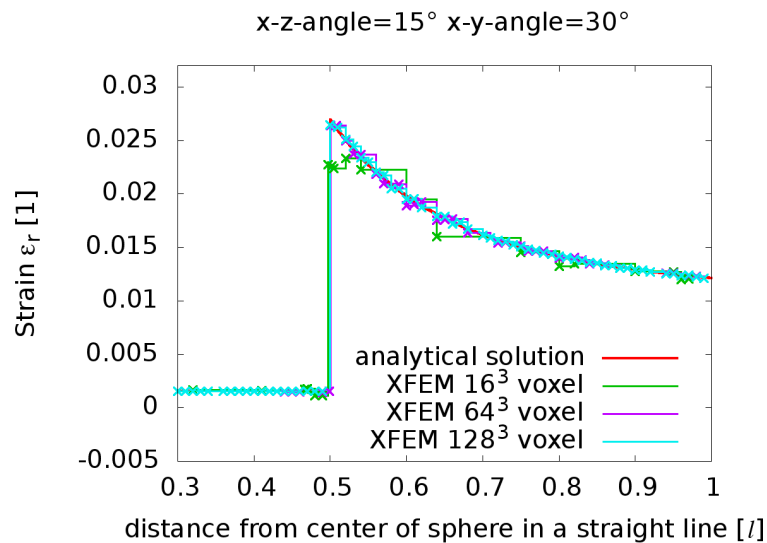

Figure 9: Normal strain component along line with x-y-angle=30° and x-z-angle=15° for XFEM

Fig. 8 and Fig. 9 show a line that is tilted by 15° away from the x axis in the x-z-plane and 30° in the x-y-plane, respectively. Fig. 8 is a good example for the standard FE method not being able to reproduce the jump in the radial strain component, independent from the mesh parameter h. Not surprising at all, the finest meshes with a mesh parameter h_4 does reproduce the jump better than the coarser meshes. An additional error is introduced as for most of the meshes in Fig. 8 there is a ramp up effect instead of a single jump. This again was also observed with different integration rules. Fig. 9 shows that the same line of Fig. 8 does not lead to problems for the XFEM. Only the coarsest mesh seems to be a bit off. Nevertheless, in both figures there are oscillations around the analytical solution observable, which was the case in all simulations.

To get a better impression on the difference between the computed result and the analytical solution let us introduce

an error measure depending on the mesh parameter h as follows.

$$\text{err}^{\text{fem/xfem}}(h) := \frac{1}{V_\Omega} \int\limits_{\Omega_h} ||u_{\text{analytical}}(x) - u_h^{\text{fem/xfem}}(x)|| \, dx. \tag{30}$$
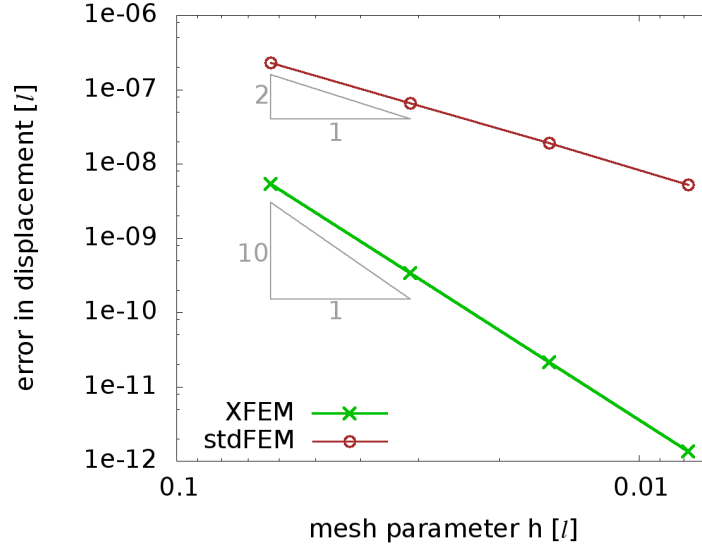

Figure 10: Error in displacement for different mesh parameters

Fig. 10 shows a log-log-plot of this integrated error over mesh parameter h introduced in Eq. 30. It strikes that the total error with the XFEM on the coarsest grid with mesh parameter h_1 is only slightly larger than the total error in the standard FEM on the finest grid analyzed. It also strikes that the convergence rate of the XFEM is drastically better that for the standard FEM. The order of convergence for the standard FEM is quadratic whereas the XFEM converges significantly faster. Nevertheless the authors want to emphasize that both XFEM and FEM will never exactly match the analytical solution. This is due to the fact that in both cases independent from the mesh size the material interface is approximated with piecewise linear elements.

4 Discussion

In this study an analytical solution for a spherical inclusion in a finite domain under specific loading conditions is considered and compared in detail to different finite element discretizations with standard FEM and XFEM. Analyzing the normal component of the strain tensor along specific lines through the material reveals that the XFEM is able to reproduce the jump in this strain component at the material interface. This is crucial when modeling more complex material behavior like interface failure and debonding. Similar to Lian et al. (2012) XFEM is not able to suppress oscillations around material interfaces completely. Nevertheless the magnitude of oscillations is reduced drastically, when using XFEM compared to standard FEM. However, when analyzing the total error of the simulations, the main result of this work becomes apparent: the XFEM converges significantly faster than standard FEM.

References

Axelsson, R. E.; Barker, V. A.: *Finite Element Solution of Boundary Value Problems*. Academic Press, London (1984).

Belytschko, T.; Black, T.: Elastic crack growth in finite elements with minimal remeshing. *International Journal for Numerical Methods in Engineering*, 45, 5, (1999), 601–620.

Belytschko, T.; Moës, N.; Usui, S.; Parimi, C.: Arbitrary discontinuities in finite elements. *International Journal for Numerical Methods in Engineering*, 50, 4, (2001), 993–1013.

Eshelby, J.: The determination of the elastic field of an ellipsoidal inclusion, and related problems. *Proceedings of the Royal Society of London. Series A. Mathematical and Physical Sciences*, 241, 1226, (1957), 376–396.

Fries, T.; Belytschko, T.: The extended/generalized finite element method: An overview of the method and its applications. *International Journal for Numerical Methods in Engineering*, 84, 3, (2010), 253–304.

Gross, D.; Hauger, W.; Schnell, W.; Wriggers, P.: *Technische Mechanik*, vol. 4. Springer, Berlin, Heidelberg, New York (1990).

Guldberg, R.; Hollister, S.; Charras, G.: The accuracy of digital image-based finite element models. *Journal of Biomechanical Engineering*, 120, 2, (1998), 289.

Lian, W.; Legrain, G.; Cartraud, P.: Image-based computational homogenization and localization: comparison between x-fem/levelset and voxel-based approaches. *Computational Mechanics*, 51, 3, (2012), 1–15.

Moës, N.; Cloirec, M.; Cartraud, P.; Remacle, J.: A computational approach to handle complex microstructure geometries. *Computer Methods in Applied Mechanics and Engineering*, 192, 28, (2003), 3163–3177.

Moës, N.; Dolbow, J.; Belytschko, T.: A finite element method for crack growth without remeshing. *International Journal for Numerical Methods in Engineering*, 46, 1, (1999), 131–150.

Mura, T.: *Micromechanics of defects in solids*, vol. 3. Springer (1987).

Osher, S.; Sethian, J.: Fronts propagating with curvature-dependent speed: algorithms based on Hamilton-Jacobi formulations. *Journal of Computational Physics*, 79, 1, (1988), 12–49.

Rutka, V.; Wiegmann, A.; Andrä, H.: EJIIM for calculation of effective elastic moduli in 3d linear elasticity. Tech. Rep. 93, Berichte des Fraunhofer ITWM 93 (2006).

Sethian, J.: *Level set methods and fast marching methods: evolving interfaces in computational geometry, fluid mechanics, computer vision, and materials science*, vol. 3. Cambridge University Press (1999).

Stolarska, M.; Chopp, D.; Moës, N.; Belytschko, T.: Modelling crack growth by level sets in the extended finite element method. *International Journal for Numerical Methods in Engineering*, 51, 8, (2001), 943–960.

Zienkiewicz, O.; Taylor, R.: *The Finite Element Method*, vol. 1. Butterworth-Heinemann, 5 edn. (2000).

Address: Tobias Zangmeister, Fraunhofer ITWM, Fraunhofer-Platz 1, 67663 Kaiserslautern
email: `tobias.zangmeister@itwm.fraunhofer.de`